arXiv:1601.07196v1 [physics.class-ph] 25 Jan 2016

2D BEM modeling of a singular thermal diffusion free boundary problem with phase change

V. S. Nikolayev & D. A. Beysens
ESEME, Service des Basses Températures, DSM/DRFMC, CEA-Grenoble, France[*]

Abstract

We report a 2D BEM modeling of the thermal diffusion-controlled growth of a vapor bubble attached to a heating surface during saturated pool boiling. The transient heat conduction problem is solved in a liquid that surrounds a bubble with a free boundary and in a semi-infinite solid heater. The heat generated homogeneously in the heater causes evaporation, i. e. the bubble growth. A singularity exists at the point of the triple (liquid-vapor-solid) contact. At high system pressure the bubble is assumed to grow slowly, its shape being defined by the surface tension and the vapor recoil force, a force coming from the liquid evaporating into the bubble. It is shown that at some typical time the dry spot under the bubble begins to grow rapidly under the action of the vapor recoil. Such a bubble can eventually spread into a vapor film that can separate the liquid from the heater, thus triggering the boiling crisis (Critical Heat Flux phenomenon).

1 Introduction

Boiling is widely used to transfer heat from a solid heater to a liquid. The bubble growth in boiling attracted much of attention from many scientists and engineers. In spite of these efforts, some important aspects of growth of a vapor bubble attached to a solid heater remain misunderstood even on a phenomenological level. The most important aspect is the boiling crisis, a transition from nucleate boiling (where vapor bubbles nucleate on the heater) to film boiling (where the heater is

[*]Mailing address: CEA-ESEME, Institut de Chimie de la Matière Condensée de Bordeaux, 87, Avenue du Dr. Schweitzer, 33608 Pessac Cedex, France

covered by a continuous vapor film). The boiling crisis is observed when the heat flux q_S from the solid heater exceeds a threshold value which is called the "Critical Heat Flux" (CHF). The rapid formation of the vapor film on the heater surface decreases steeply the heat transfer efficiency and leads to a local heater overheating. In the industrial heat exchangers, the boiling crisis can lead to melting of the heater thus provoking a dangerous accident. Therefore, the knowledge of the CHF is extremely important. However, the CHF depends on many parameters. At this time, there are several semi-empirical correlations that predict the CHF more or less reliably for several particular regimes of boiling and heater configurations, see [1] for a recent review. However, a clear understanding of the triggering mechanism of the boiling crisis is still lacking.

The knowledge about what happens at the foot of the bubble which grows attached to the heater is crucial for the correct modeling of the boiling crisis. Unfortunately, the experimental observations at large heat fluxes close to the CHF are complicated by the violence of boiling and optical distortions caused by the strong temperature gradients. We proposed recently [2] to carry out boiling experiments in the proximity of the critical point where the CHF is very small and the bubble evolution is very slow. However, microgravity conditions are necessary in this case to obtain a convex bubble shape in order to observe a behavior similar to the terrestrial boiling.

The bubble foot contains the contact line of the bubble with the heater. This triple solid-liquid-gas contact line is a line of singularity points both for the hydrodynamic (see [3] and refs. therein) and for the heat conduction problems. In the present article we consider only the heat conduction part by assuming the slow growth and the quasi-static bubble shape which is common for the high pressure boiling. The results of such a calculation have already been described in [5]. The present article deals with the problem framework and some calculation details related to BEM.

2 Boundary conditions for the contact line problem

The choice of the boundary conditions adopted in the contact line is very important. Since the contact line is triple, boundary conditions should be specified at three surfaces that intersect there (Fig. 1). For the gas-liquid interface, we adopt the constant-temperature boundary condition with the temperature that corresponds to the saturation temperature T_{sat} for the given (constant) system pressure. The gas phase is assumed to be non-conductive, the heat flux through the solid-gas interface being zero. The boundary condition on the solid-liquid interface remains to be defined. It is the subject of the rest of this section.

There are three kinds of boundary conditions. Let us consider them on an example of the 2D wedge geometry as illustrated in Fig. 1 for which some important solutions can be obtained in analytical form.

Since the heater is a far better heat conductor than the liquid, the constant temperature boundary condition ($T = T_S$ =const along the solid-liquid interface) seems natural. In order to maintain boiling, $T_S > T_{sat}$ should be satisfied. The

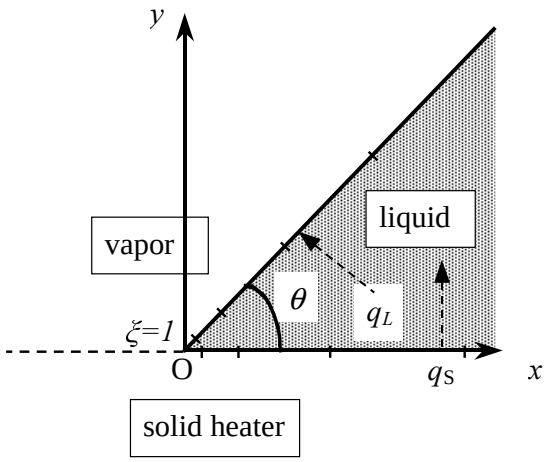

Figure 1: Geometry for the calculation of the heat conduction in the wedge geometry. The BEM discretization of the wedge is also illustrated.

resulting problem is ill posed because the temperature is discontinuous along the boundary of the liquid domain at the contact point O in Fig. 1. This discontinuity leads to a singular behavior of the heat flux q_L through the gas-liquid boundary, $q_L(y) \propto y^{-1}$ [4] and is not integrable. Note that the integral $\int q_L \mathrm{d}y$ is very important because it defines the amount of liquid evaporated into the bubble and thus the bubble growth rate, see Eq. (11) below. Since the result is infinite, the first kind boundary condition cannot be used.

Another choice is the constant heat flux q_S along the solid-liquid interface, which can be reasonable for a thin heater. The resulting transient problem can be solved analytically in the liquid domain by the reflections method [4]. Its solution can be obtained in the closed form for several contact angles θ, see Fig. 1. The solutions obtained in [5] for $\theta = \pi/4$ and $\theta = \pi/8$ result in a constant value for $q_l(y \to 0)$. Although the solution for $\theta = \pi/2$ diverges $q_L(y) \propto \log(-y)$ [6], it is integrable. In spite of these advantages, the constant heat flux boundary condition is not suitable for the bubble growth problem because it cannot be used in the dry spot (i. e. solid-gas contact) area where the heat flux should be zero. However, these analytical solutions can be used to test the BEM solver code (see Fig. 2).

A remaining option is the boundary conditions of a third kind, i.e. the coupling of the temperatures and the fluxes at the solid surface. The heat conduction problem is required to be solved in the solid domain in addition to the liquid domain. Unfortunately, we cannot solve the problem analytically in this case. Qualitatively, one can expect an integrable divergence of $q_L(y)$ which should appear because of the influence of the solid-gas contact area adjacent to the contact line. Since the heat flux that comes from the bulk of the solid heater is not able to pass through this area, it should be necessarily deviated towards the neighboring solid-liquid

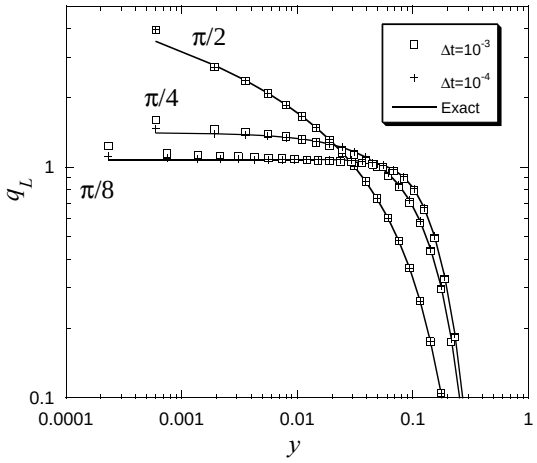

Figure 2: The $q_L(y)$ curves calculated for the $\pi/2$, $\pi/4$ and $\pi/8$ wedges for the values of the parameters $q_0 = 1$, $\alpha_L = 1$, $t = 0.01$ and $d_{min} = 0.001$ and two values of the time step Δt. The results of the numerical solution by BEM (data points) should be compared with the exact analytical solutions (lines).

contact area thus increasing q_S at small x. Since $q_S \approx q_L$ near the contact line, $q_L(y)$ should vary steeper near the contact line than in the constant q_S case and is likely to diverge.

One can argue that the necessity of the calculation of the temperature field in the heater is a heavy complication that justifies the approximation of the simultaneous application of the boundary conditions of constant heat flux outside the dry spot and zero heat flux inside. However, the above considerations show that the behavior of $q_L(y)$ can deviate from its real behavior even qualitatively. Since such a large error cannot be admitted in the calculation of q_L that strongly influences the bubble dynamics, we need to calculate rigorously the conjugate heat conduction problem.

3 Mathematical problem statement

The 2D heat conduction problem in the domain $\Omega_L \cup \Omega_S$ (see Fig. 3) reads

$$\frac{\partial T_L}{\partial t} = \alpha_L \nabla^2 T_L, \quad \vec{r} \in \Omega_L \tag{1}$$

$$\frac{\partial T_S}{\partial t} = \alpha_S \nabla^2 T_S + \frac{\alpha_S}{k_S} j(t), \quad \vec{r} \in \Omega_S \tag{2}$$

where α and k is the thermal diffusivity and conductivity respectively, the indices L and S identify the liquid and the solid heater, and $\vec{r} = (x, y)$ denotes a point. The

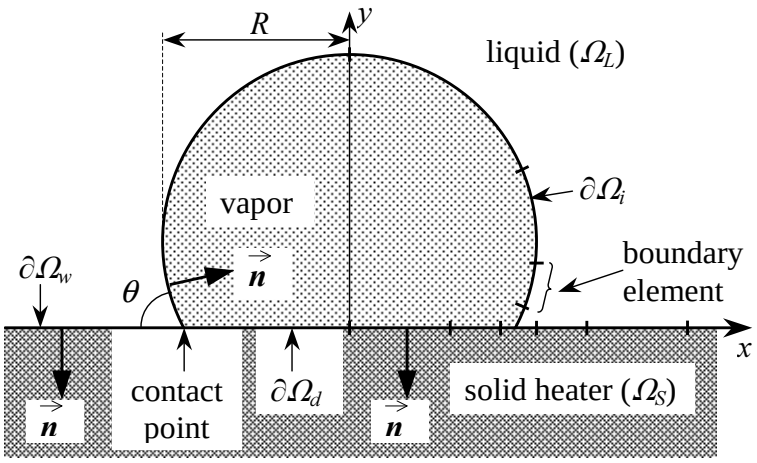

Figure 3: Vapor bubble on the heater (domain Ω_S) surrounded by the liquid (domain Ω_L). The chosen direction of the unit normal vector $\vec{n}$ is shown for each of the subcontours $\partial\Omega_w$, $\partial\Omega_d$ and $\partial\Omega_i$. The discretization is illustrated for the right half of the subcontours. (From [5] with permission from Elsevier Science)

heat is assumed to be generated homogeneously in the heater with the power $j(t)$ per unit volume. We choose $j(t) = C/\sqrt{t}$, where C is constant. This condition results in a constant in time value of q_S far from the bubble, see (14) below. Initially $(t = 0)$ the temperature is homogeneous $T_L = T_S = T_{sat}$. The vapor bubble is assumed to be already nucleated. Since we assume the zero contact angle $\theta = 0$, the bubble shape is spherical with the radius R_0. The boundary conditions are formulated on the moving gas-liquid interface $\partial\Omega_i$ ($T_L|_{\partial\Omega_i} = T_{sat}$), on the solid-liquid interface $\partial\Omega_d$ ($\partial T_L/\partial y|_{\partial\Omega_d} = 0$) and on the solid-liquid interface $\partial\Omega_w$:

$$\begin{aligned} q_S &= -k_S \left.\frac{\partial T_S}{\partial y}\right|_{\partial\Omega_w} = -k_L \left.\frac{\partial T_L}{\partial y}\right|_{y=0}, \\ T_S|_{\partial\Omega_w} &= T_L|_{y=0}\,. \end{aligned} \tag{3}$$

Because of the axial symmetry, this problem needs to be solved only for $x > 0$.

The shape of the gas bubble is calculated from the quasi-static equation [6]

$$K(\vec{r}_i)\sigma = \lambda + P_r(\vec{r}_i), \tag{4}$$

where K is the curvature of the bubble at the point on the surface $\vec{r}_i = (x_i, y_i)$, σ is the vapor-liquid interface tension and λ is a constant difference of pressures between the vapor and the liquid. The vapor recoil pressure

$$P_r(\vec{r}_i) = [q_L(\vec{r}_i)/H]^2(\rho_V^{-1} - \rho_L^{-1}), \tag{5}$$

where $q_L = -k_L(\vec{n}\cdot\nabla)\,T_L|_{\partial\Omega_i}$ appears due to the uncompensated momentum of vapor molecules that leave the interface. The latent heat of vaporization is denoted by H, ρ_V and ρ_L being the vapor and liquid densities. Eq. (4) is convenient to solve when the bubble contour is described in parametric form $\vec{r}_i = \vec{r}_i(\xi)$ where ξ is the distance from the topmost point of the bubble to the point $\vec{r}_i$ measured along the bubble contour. When ξ is non-dimensionalized by the half-length of the bubble contour L, $\xi = 1$ corresponds to the contact point and (4) becomes equivalent to the following set of ODEs [5]:

$$\mathrm{d}x_i/\mathrm{d}\xi = L\cos u, \tag{6}$$

$$\mathrm{d}y_i/\mathrm{d}\xi = -L\sin u, \tag{7}$$

$$\mathrm{d}u/\mathrm{d}\xi = L(\lambda + P_r(\xi))/\sigma \tag{8}$$

were $u = u(\xi)$ is an auxiliary function. The boundary conditions for this set read $x_i(0) = 0$, $u(0) = 0$, $y_i(1) = 0$. By fixing the contact angle $u(1) = \pi - \theta$ one can determine the unknown L from (8),

$$L = (\pi - \theta)\sigma \left[\int_0^1 P_r(\xi)\mathrm{d}\xi + \lambda\right]^{-1}, \tag{9}$$

$\theta = 0$ is assumed in the rest of this article. The constant λ should be determined using the known volume V of the 2D bubble,

$$V = -\frac{1}{2}\int\limits_{(\partial\Omega_i)} (x_i n_x + y_i n_y)\,\mathrm{d}\,\partial\Omega, \tag{10}$$

where n_x and n_y are the components of $\vec{n}$, Fig. 3. The bubble volume increases in time due to evaporation at $\partial\Omega_i$

$$H\rho_V\frac{\mathrm{d}V}{\mathrm{d}t} = \int\limits_{(\partial\Omega_i)} q_L(\vec{r}_i)\,\mathrm{d}\,\partial\Omega, \tag{11}$$

This equation is used widely to describe the thermally controlled bubble growth. The initial condition is $V(t=0) = 4/3\,\pi R_0^3$.

The problem (1-11) is now complete. It can be solved by BEM. However, it is not convenient to solve by BEM because the temperature and its gradient are both non-zero at infinity (more precisely, at $x \to \infty$), where the closing subcontours for the domains Ω_L and Ω_S are located. We solve this problem easily by subtracting the solutions at $x \to \infty$. These solutions for the both domains read [5]

$$T_L^{inf} = T_{sat} + \frac{q_0}{k_L}\left[\sqrt{\frac{4\alpha_L t}{\pi}}\exp\left(-\frac{y^2}{4\alpha_L t}\right) - y\,\mathrm{erfc}\left(\frac{y}{2\sqrt{\alpha_L t}}\right)\right], \tag{12}$$

$$T_S^{inf} = T_{sat} + \frac{2\alpha_S}{k_S}C\sqrt{t} -$$

$$\frac{q_0}{k_S}\left[\sqrt{\frac{4\alpha_S t}{\pi}}\exp\left(-\frac{y^2}{4\alpha_S t}\right)+y\,\mathrm{erfc}\left(-\frac{y}{2\sqrt{\alpha_S t}}\right)\right], \tag{13}$$

where $\mathrm{erfc}(\cdot)$ is the complementary error function [7]. As one can easily find, the flux from the heater q_0 far from the bubble

$$q_0 \equiv q_S(x\to\pm\infty) = C\sqrt{\pi}\alpha_S k_L/(k_S\sqrt{\alpha_L}+k_L\sqrt{\alpha_S}), \tag{14}$$

is constant in time. We use its value as a control parameter instead of C.

By introducing the characteristic scales for time (Δt, the time step), length (R_0, the initial bubble radius), heat flux ($\bar{q}$), and thermal conductivity ($\bar{k}$), all other variables can be made non-dimensional. In particular, the characteristic temperature scale in the system is $\bar{q}R_0/\bar{k}$. The following four non-dimensional groups define completely the behavior of the system

$$\mathrm{Fo}_{L,S} = \alpha_{L,S}\Delta t/R_0^2 \text{ — Fourier numbers,}$$

$$\mathrm{Ja} = \frac{k_L\bar{q}R_0}{\rho_V H\bar{k}\alpha_L} \text{ — Jakob number,}$$

$$\mathrm{Hi} = \frac{R_0\,\bar{q}^2}{\sigma H^2}(\rho_V^{-1}-\rho_L^{-1}) \text{ — Hickman number,}$$

together with the non-dimensionalized values of q_0 and $k_{L,S}$. The non-dimensional heat transfer problem can now be formulated in terms of temperatures $\psi_{L,S} = (T_{L,S}-T_{L,S}^{inf})/(\bar{q}R_0/\bar{k})$ and fluxes $\zeta_{L,S} = k_{L,S}\,\partial\psi_{L,S}/\partial\vec{n}$.

4 Numerical implementation

4.1 BEM formulation

Since $\psi_{L,S} = \zeta_{L,S} = 0$ at infinity, the heat conduction problem is equivalent to a set of two BEM equations [8] for the open integration contours $\partial\Omega_L = \partial\Omega_i \cup \partial\Omega_w$ and $\partial\Omega_S = \partial\Omega_d \cup \partial\Omega_w$. Using $t = 0$ as the initial time moment and taking into account that $\psi_{L,S}(t=0) = 0$ so that the volume integral disappears, these equations read

$$\int_0^{t_F}\mathrm{d}t\int_{(\partial\Omega_{L,S})}\left[G^{L,S}(\vec{r'},t_F;\vec{r},t)\left(\mathrm{Fo}_{L,S}\frac{\zeta_{L,S}(\vec{r},t)}{k_{L,S}}+\psi_{L,S}(\vec{r},t)v^n(\vec{r},t)\right)-\right.$$

$$\left.\mathrm{Fo}_{L,S}\,\psi_{L,S}(\vec{r},t)\frac{\partial_r G^{L,S}(\vec{r'},t_F;\vec{r},t)}{\partial\vec{n}_r}\right]\mathrm{d}_r\partial\Omega = \frac{1}{2}\psi_{L,S}(\vec{r'},t_F), \tag{15}$$

where the point $\vec{r'}$ belongs to $\partial\Omega_{L,S}$ respectively, v^n is the normal component of the contour velocity (nonzero only on $\partial\Omega_i$) and

$$G^{L,S}(\vec{r'},t_F;\vec{r},t) = \frac{1}{4\pi\mathrm{Fo}_{L,S}(t_F-t)}\exp\left[-\frac{|\vec{r'}-\vec{r}|^2}{4\,\mathrm{Fo}_{L,S}(t_F-t)}\right]. \tag{16}$$

In the following, the indices L and S for all variables in the equations will be dropped for the sake of clarity.

The constant element BEM [9] was used, i. e. both ζ and ψ were assumed to be constant during any time step and on any element $\partial\Omega_j$, their values on the element being associated with the values at the node B_j in the middle of the element approximated by a straight segment that joins its ends M_{j-1} and M_j. The time steps are equal, i.e. $t_f = f$. The values of ζ and ψ on the element j at time f are denoted by ζ_{fj} and ψ_{fj}. Each of the integral equations (15) reduces to the system of linear equations

$$\sum_{f=1}^{F}\sum_{j=1}^{2N_f}[(\zeta_{fj}/k + \psi_{fj}v^n_{fj}/\mathrm{Fo})G^{Ff}_{ij} - \psi_{fj}H^{Ff}_{ij}] = \psi_{Fi}/2, \tag{17}$$

where N_f is the number of elements on one half of the integration contour at time step f, F_{max} is the maximum calculation time; $i = 1 \dots 2N_F$ and $F = 1 \dots F_{max}$; H_{ij} and G_{ij} are the BEM coefficients:

$$\begin{aligned} G^{Ff}_{ij} &= \mathrm{Fo}\int\limits_{f-1}^{f}\mathrm{d}t\int\limits_{(\partial\Omega_j)} G(\vec{r}_i, F; \vec{r}, f)\mathrm{d}_r\partial\Omega, \\ H^{Ff}_{ij} &= \mathrm{Fo}\int\limits_{f-1}^{f}\mathrm{d}t\int\limits_{(\partial\Omega_j)} \frac{\partial G(\vec{r}_i, F; \vec{r}, f)}{\partial\vec{n}_r}\mathrm{d}_r\partial\Omega. \end{aligned} \tag{18}$$

Since the calculation of these coefficients takes the most of computation time, it should be made fast.

4.2 Algorithm for the BEM coefficients

The value of each particular BEM coefficient for the element $\partial\Omega_j = (M_{j-1}, M_j)$ of the length l is calculated using the coordinate transformation [11] to the Cartesian system where B_j is the reference point and the x axis is directed toward M_{j-1}. The direction of the normal vector $\vec{n}$ coincides with the y axis. The time integration [9] results in

$$G^{Ff}_{ij} = \int\limits_{-l/2}^{l/2}\frac{1}{4\pi}\left[E_1\left(\frac{(x+u)^2+y^2}{4\,\mathrm{Fo}(F-f+1)}\right) - E_1\left(\frac{(x+u)^2+y^2}{4\,\mathrm{Fo}(F-f)}\right)\right]\mathrm{d}u, \tag{19}$$

$$H^{Ff}_{ij} = \int\limits_{-l/2}^{l/2}\frac{y}{2\pi}\left[\frac{\exp\left(-\frac{(x+u)^2+y^2}{4\,\mathrm{Fo}(F-f+1)}\right)}{(x+u)^2+y^2} - \frac{\exp\left(-\frac{(x+u)^2+y^2}{4\,\mathrm{Fo}(F-f)}\right)}{(x+u)^2+y^2}\right]\mathrm{d}u, \tag{20}$$

where (x, y) denote the coordinates of the point $\vec{r}_i$ in the new reference system and $E_1(\cdot)$ is the exponential integral [7]. The situation $i = j$ (i.e. where $x = y = 0$) is particular, which is a quite general feature of BEM.

4.2.1 G coefficient

Note that the case $f = F$ for (19) is not singular, the second term of the integrand in (19) being zero. Therefore, we will deal only with this case. The integration of the second term that exists when $f < F$ is similar to the first.

The divergence of $E_1(z)$ at $z \to 0$ is logarithmic and thus integrable. Usually this means that the integration can be performed by the Gauss method. However, since our problem is singular due to the contact line effects, many Gauss points are needed to attain the required accuracy in the contact line region and a more sophisticated algorithm is necessary to get both accuracy and speed. The analytical integration [10] is used when $y = 0$ i.e. when the singularity occurs. Although there is no singularity when $y \neq 0$, the integrand varies sharply near the point $u = -x$ when $y \ll l$. For the case $|x| < l/2$, the integration interval can be split by the point $u = -x$ and changes of variables can be done in both integrals to produce

$$G_{ij}^{FF} = \frac{\sqrt{\mathrm{Fo}}}{4\pi} \left\{ \int_{y^2/4\mathrm{Fo}}^{[(x+l/2)^2+y^2]/4\mathrm{Fo}} \frac{E_1(z)}{\sqrt{z - y^2/4\mathrm{Fo}}}\,\mathrm{d}z + \int_{y^2/4\mathrm{Fo}}^{[(x+l/2)^2+y^2]/4\mathrm{Fo}} \frac{E_1(z)}{\sqrt{z - y^2/4\mathrm{Fo}}}\,\mathrm{d}z \right\}. \tag{21}$$

At first glance, no advantage is obtained because of the divergence. However, the approximation [7] of $E_1(z)$ for $z < 1$ allows the analytical integration to be performed term by term and results in

$$\begin{aligned} \int_b^a \frac{E_1(z)}{\sqrt{z-b}}\,\mathrm{d}z = -4\sqrt{b}\arctan\sqrt{\frac{a-b}{b}} + 2\sqrt{a-b}\,[1.422784 - \log(a) + \\ 0.333331\,(a+2b) - 0.0166607\,(3a^2+4ab+8b^2) + \\ 1.577134\cdot 10^{-3}\,(5a^3+6a^2b+8ab^2+16b^3) - \\ 3.09843\cdot 10^{-5}(35a^4+40a^3b+48a^2b^2+64ab^3+128b^4) + \\ 1.55638\cdot 10^{-6}(63a^5+70a^4b+80a^3b^2+96a^2b^3+128ab^4+256b^5)] \end{aligned} \tag{22}$$

where $b \leq a < 1$ are assumed. For the remaining part of the integration interval, the 8-point Gauss integration is performed and gives a sufficient accuracy.

The case $|x| > l/2$ should be solved similarly when the argument of E_1 in (19) can be less than unity somewhere in the integration interval.

4.2.2 H coefficient

The value of the coefficient (19) at $y = 0$ is zero. While no singularity exists when $f < F$ (this case can be integrated by Gauss method), the function

$$H_{ij}^{FF} = \frac{y}{2\pi} \exp\left(-\frac{y^2}{4\,\mathrm{Fo}}\right) \int\limits_{x-l/2}^{x+l/2} \frac{\exp\left(-\frac{u^2}{4\,\mathrm{Fo}}\right)}{u^2+y^2}\,\mathrm{d}u \tag{23}$$

is discontinuous at $y = 0$. The integration interval in (23) contains the point $u = 0$ when $|x| < l/2$. Since the integrand is an even function of u, this integral can be presented as

$$\int\limits_{x-l/2}^{x+l/2} \ldots = \int\limits_{0}^{x+l/2} \ldots + \int\limits_{0}^{l/2-x} \ldots$$

and the interval $(0, \varepsilon)$, where $0 < \varepsilon \ll l/2$, can be separated out of the both integrals. The contribution of this interval to (23) turns out to be

$$H_{ij}^{FF} = \frac{1}{\pi} \exp\left(-\frac{y^2+\varepsilon^2/4}{4\,\mathrm{Fo}}\right) \arctan\frac{\varepsilon}{y} + \ldots$$

The discontinuity is evident now: while $y \to +0$ limit is $1/2$, the value at $y = 0$ is zero and $y \to -0$ limit is $-1/2$.

After the integration over the interval $(-\varepsilon, \varepsilon)$ analytically, the Gauss method can be employed to integrate over the remaining parts of the interval in (23).

4.3 Calculation scheme

The system (17) can be simplified due to axial symmetry of the problem $\zeta, \psi_{fj} = \zeta\psi_{f(2N_f-j)}$:

$$\sum_{f=1}^{F}\sum_{j=1}^{N_f}[(\zeta_{fj}/k + \psi_{fj}v_{fj}^n/\mathrm{Fo})\tilde{G}_{ij}^{Ff} - \psi_{fj}\tilde{H}_{ij}^{Ff}] = \psi_{Fi}/2, \tag{24}$$

where $i = 1 \ldots N_F$, $F = 1 \ldots F_{max}$, $\tilde{G}_{ij}^{Ff} = G_{ij}^{Ff} + G_{i(2N_f-j)}^{Ff}$ and $\tilde{H}_{ij}^{Ff} = H_{ij}^{Ff} + H_{i(2N_f-j)}^{Ff}$. Unfortunately, no effective time marching scheme [9] can be applied because of the free boundaries. The position of each node depends on time. Therefore, it is very important that $\tilde{G}_{ij}^{Ff}$ be calculated using the coordinates of the i-th point at time moment F and those of j-th point at time moment f.

Our 2D BEM algorithm was tested for the fixed boundary wedge problem (for the Ω_L domain only) with the constant heat flux boundary condition described in section 2. Since ζ decreases to zero far from the contact point, integration contour can be closed at the distance $x_{max} \sim 10\sqrt{\mathrm{Fo}\,t}$ from the contact point O$(0,0)$ where $\zeta(x,y,t)$ is sufficiently small. The element lengths grow exponentially ($d_{min}, d_{min}e^b, d_{min}e^{2b}, \ldots$) from the contact point into each of the sides of

the wedge (see Fig. 1), where b is fixed at 0.2. Since x_{max} increases with time, the total number of the elements also increases during the evolution of the bubble. Being an input parameter, d_{min} is adjusted slightly on each time step to provide the exponential growth law for the elements on the interval with the fixed boundaries $(0, x_{max})$. Remeshing on each time step was performed to comply with the free boundary nature of the main problem where the remeshing is mandatory.

The results for $\theta = \pi/8,\ \pi/4$ and $\pi/2$ are shown in Fig. 2 to be compared with the analytical solutions [5, 6]. It is easy to see that the method produces excellent results except for the element closest to the contact point. The algorithm overestimates the value of q_L at this element. The error is larger for the $\pi/2$ wedge, for which $q_L \to \infty$ at the contact point. We verified that the influence of the increase of the time and space steps on the numerical error is very weak.

The discretization of the integration subcontours of the bubble growth problem $\partial\Omega_w$, $\partial\Omega_d$ and $\partial\Omega_i$ follows the same exponential scheme (see Fig. 3) that was used for the discretization of the wedge sides in the test example above. Since the free boundary introduces a nonlinearity into the problem, the following iteration algorithm is needed to determine the bubble shape on each time step [8]:

1. Shape of the bubble is guessed to be the same as on the previous time step;
2. The variations of v^n and P_r along the bubble interface are guessed to be the same as on the previous time step;
3. Discretization of the contours $\partial\Omega_w$, $\partial\Omega_d$ and $\partial\Omega_i$ is performed;
4. Temperatures and fluxes on the contours $\partial\Omega_w$, $\partial\Omega_d$ and $\partial\Omega_i$ are found by solving (24) for $\psi, \zeta_{L,S}$ at the time moment F;
5. Volume V and vapor recoil P_r are calculated using (11) and (5);
6. Bubble shape is determined for the calculated values of V and P_r;
7. If the calculated shape differs too much from that on the previous iteration, the velocity of interface v^n is calculated, and steps 3 – 7 are repeated until the required accuracy is attained.

As a rule, three iterations give the 0.1% accuracy which is sufficient for our purposes.

The normal velocity of interface v^n_{Fi} at the time F and at node i is calculated using the expression

$$v^n_{Fi} = (x_{Fi} - x_{(F-1)j})n^x_{(F-1)j} + (y_{Fi} - y_{(F-1)j})n^y_{(F-1)j}, \qquad (25)$$

where x_{Fi} is the coordinate of the node i at time F, and j is the number of the node (at time $F-1$) geometrically closest to (x_{Fi}, y_{Fi}).

The system of Eqs. 6 – 8 is solved by direct integration. The integration of the right-hand side of (8) is performed using the simple mid-point rule, because the values of P_r are calculated at the mid-points (nodes) only. The subsequent integration of the right-hand sides of Eqs. 6 – 7 is performed using the Simpson rule (to gain accuracy) for the non-equal intervals. The trapezoidal rule turns out to be accurate enough for the calculation of volume in (10). For the simulation we used the parameters for water at 10 MPa pressure on the heater made of stainless steel listed in [5].

The above described algorithm should give good results when $\int_0^1 P_r(\xi)\mathrm{d}\xi$ exists (cf. Eq. 9). In our case $P_r(\xi)$ can be approximated by the power function $(1-\xi)^{-2\beta}$ when $\xi \to 1$. The exponent β, which comes from the approximation for $q_L(\xi)$, turns out to be larger than one half (see discussion in the next section). Thus if the data were extrapolated to the contact point $\xi = 1$, this integral would diverge. We note, however, that the evaporation heat flux is limited [12] by a flux q_{max} which is about 10^4 MW/m^2 for the chosen parameters.

The q_L divergence is originated from the assumption that the temperature remains constant along the vapor-liquid interface. In reality, this assumption is violated in the very close vicinity of the contact point where the heat flux q_L is comparable to q_{max}. Thus we accept the following approximation for the function $q_L(\xi)$, $\xi < 1$. It is extrapolated using the power law $q_L(\xi) \propto (1-\xi)^{-\beta}$ until it reaches the value of q_{max} and remains constant while ξ increases to unity. This extrapolation is used to calculate the integrals in (11) and (9). There is no need to modify the constant-temperature boundary condition for the heat transfer calculations because the calculated heat flux q_L remains always less than q_{max}.

5 Results of the numerical calculation

The calculations show that the function $q_L(\xi)$ (see Fig. 4) can be described well by

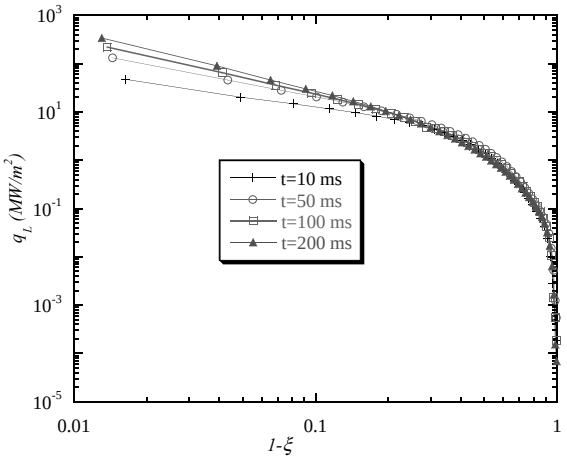

Figure 4: Variation of the heat flux q_L calculated for $q_0 = 0.05$ MW/m^2 along the bubble contour for different moments of time. The curvilinear coordinate ξ varies along the bubble contour; $\xi = 1$ at the contact point. (Reprinted from [5] with permission from Elsevier Science)

the above power law where $\beta \sim 1$ grows slightly with time. As expected, for this conjugate heat conduction problem the divergence is stronger than for the wedge

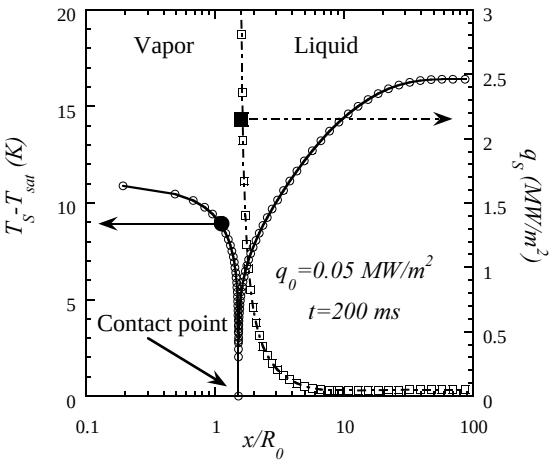

Figure 5: Variation of the heat flux q_S and the temperature T_S along the surface of the heater for $q_0 = 0.05$ MW/m^2, $t = 200$ ms. The point $x = 0$ corresponds to the center of the bubble. (Reprinted from [5] with permission from Elsevier Science)

model, Fig. 2. The difference between these two cases is caused by the behavior of the heat flux q_S in the vicinity of the contact point. While it was imposed to be uniform for the wedge, the function $q_S(x)$ increases strongly near the contact point for the conjugate heat conduction, see Fig. 5. As expected, the value of q_S on the liquid side in the vicinity of the contact line is very close to q_L, the heat flux that produces evaporation on the vapor-liquid interface and that diverges on the contact line (see Fig. 4). At some distance from the bubble center q_S reaches the value of q_0, the flux at infinity. Note that the Fig. 5 corresponds to the quasi-spherical bubble shape (see Fig. 6a) and the visible bubble radius (see Fig. 3 for the definition) $R \sim 7R_0$, so that the heat flux q_S is virtually homogeneous outside the bubble.

The variation of the temperature along the heating surface $T_S(x)$ is also shown in Fig. 5. Far from the bubble, $T_S = T_S^{inf}$ has to increase with time independently of x according to (13). It decreases to T_{sat} near the contact point because the temperature should be equal to T_{sat} on the whole vapor-liquid interface, according to the imposed boundary condition. Inside the dry spot, T_S increases with time because the heat transfer through the dry spot is blocked. It is smaller than T_S^{inf} while the dry spot under the bubble remains much smaller than R. Since q_L grows with time, at some time moment the vapor recoil pressure $P_r \propto q_L^2$ overcomes the surface tension (cf. Eq. 4) and the dry spot begins to grow, see Fig. 6b. This bubble spreading was observed experimentally in several works, e. g. [2]. The spreading bubble serves as a nucleus for the formation of a continuous vapor film that separates the solid from the liquid, i. e. triggers the boiling crisis. The heat

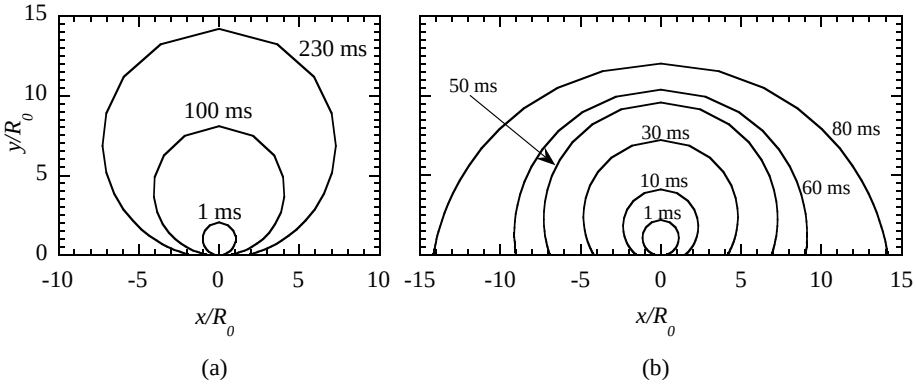

Figure 6: The bubble shape shown for the different growth times.
a) $q_0 = 0.05$ MW/m^2; b) $q_0 = 0.5$ MW/m^2.
(Reprinted from [5] with permission from Elsevier Science)

transfer becomes blocked at a larger portion of the solid surface (i.e. dry spot) and its temperature grows faster than T_S^{inf}. This temperature increase leads to the burnout of the heater observed during the boiling crisis.

6 Conclusions

Several conclusions can be made. Our analysis of the bubble growth dynamics shows the strong coupling of the heat conduction in the liquid and in the solid heater. Therefore, only a conjugate heat transfer calculation of the bubble growth can properly simulate the boiling crisis. We show that BEM suits well for such a simulation. We carried out a 2D BEM calculation. It shows that the vapor recoil can be at the origin of the boiling crisis. We demonstrated how a vapor bubble spreads over the heating surface thus initiating the boiling crisis.

Acknowledgements

We gratefully acknowledge a permission of Elsevier Science B. V. to reproduce some figures from [5]. We thank our colleagues H. Lemonnier, J. Hegseth and G.-L. Lagier for the fruitful discussions.

References

[1] Dhir, V.K., Boiling Heat Transfer, *Annu. Rev. Fluid. Mech.*, **30**, pp. 365–401, 1998.
[2] Garrabos, Y., Lecoutre-Chabot, C., Hegseth, J., Nikolayev, V.S., Beysens, D.,

Gas spreads on a heated wall wetted by liquid, *Phys. Rev. E*, **64**, pp. 051602-1–10, 2001.
[3] Andrieu, C., Beysens, D., Nikolayev, V.S., Pomeau, Y., Coalescence of sessile drops, *J. Fluid. Mech.*, **453**, pp. 427–438, 2002.
[4] Carslaw, H.S. & Jaeger, J.C., *Conduction of Heat in Solids* (2nd Edn), University Press: Oxford, 1959.
[5] Nikolayev V.S., Beysens D. A., Lagier G.-L., Hegseth J., Growth of a dry spot under a vapor bubble at high heat flux and high pressure, *Int. J. Heat Mass Transfer* **44**, pp. 3499–3511, 2001.
[6] Nikolayev, V.S., Beysens, D.A., Boiling crisis and non-equilibrium drying transition, *Europhys. Lett.*, **47**, pp. 345–351, 1999.
[7] *Handbook of Mathematical Functions*, eds. M. Abramovitz & I. A. Stegun, Natl. Bureau of Standartds, Dover, New York (1972).
[8] DeLima-Silva, W. & Wrobel, L. C., A front-tracking BEM formulation for one-phase solidification/melting problems, *Engineering Analysis with Boundary Elements*, **16**, pp. 171–182, 1995.
[9] Pina, H.L.G. & Fernandes, J.L.M., Applications in Transient Heat Conduction. *Topics in Boundary Element Research, Vol.1, Basic Principles and Applications* ed. C.A. Brebbia, Springer-Verlag, Berlin, pp. 41–58, 1984.
[10] Lagier, G.-L., Application de la méthode des élements de frontière à la résolution de problèmes de thermique inverse multidimensionnels (Application of the BEM to multidimensional inverse heat conduction problems), Ph. D. Thesis, l'Institut National Polytechnique de Grenoble, Grenoble, 1999.
[11] Hess, J.L. & Smith, A.M.O., Calculation of potential flow about arbitrary bodies, *Progress in Aeronautical Sciences, Vol.8* ed. D. Küchemann, Pergamon, 1967.
[12] Carey, van P., *Liquid-Vapor Phase Change Phenomena*, Hemisphere: Washington D.C., 1992.